Canalization of circuit assembly by δ-protocadherins in the zebrafish optic tectum

Sayantanee Biswas[1], Michelle R. Emond[1], Grace S. Philip[1] and James D. Jontes[1,*]

[1]Department of Biological Chemistry and Pharmacology
Ohio State University Wexner College of Medicine
Columbus, OH 43210

*corresponding author: jontes.1@osu.edu

Abstract

Neurons are precisely and reproducibly assembled into complex networks during development. How genes collaborate to guide this assembly remains an enduring mystery. In humans, large numbers of genes have been implicated in neurodevelopmental disorders that are characterized by variable and overlapping phenotypes. The complexity of the brain, the large number of genes involved and the heterogeneity of the disorders makes understanding the relationships between genes, development and neural function challenging. Waddington suggested the concept of canalization to describe the role of genes in shaping developmental trajectories that lead to precise outcomes[1] . Here, we show that members of the δ-protocadherin family of homophilic adhesion molecules, Protocadherin-19 and Protocadherin-17, contribute to developmental canalization of visual circuit assembly in the zebrafish. We provided oriented visual stimuli to zebrafish larvae and performed *in vivo* 2-photon calcium imaging in the optic tectum. The latent dynamics resulting from the population activity were confined to a conserved manifold. Among different wild type larvae, these dynamics were remarkably similar, allowing quantitative comparisons within and among genotypes. In both Protocadherin-19 and Protocadherin-17 mutants, the latent dynamics diverged from wild type. Importantly, these deviations could be averaged away, suggesting that the loss of these adhesion molecules leads to stochastic phenotypic variability and introduced disruptions of circuit organization that varied among individual mutants. These results provide a specific, quantitative example of canalization in the development of a vertebrate neural circuit, and suggest a framework for understanding the observed variability in complex brain disorders.

33   ***Introduction***

34   Despite their immense complexity, vertebrate brains are highly organized and exhibit a

35   conserved, stereotyped architecture. Distinct brain regions comprise canonical circuits that carry out

36   well-defined functions, which are conserved both within and between species[2,3] . The assembly of these

37   conserved circuits is robust to genetic and environmental variation, as well as natural biological

38   heterogeneity. This allows the brains of distinct individuals to perform the same tasks, even though they

39   are not identical at the level of neurons and synapses, or in their particular developmental histories. The

40   mechanisms that confer robust circuit development in the face of these multiple sources of variability are

41   poorly understood[4,5] .

42   In the case of neurodevelopmental disorders, such as schizophrenia and autism, the relationship

43   between conserved structure and conserved function breaks down. Characterized by profound

44   disturbances in normal brain function, some evidence suggests that these disorders are

45   "connectopathies," arising from disruption of the underlying network topology[6–10] . While a large number

46   of genes have been linked to developmental brain disorders, understanding the relationship of genotype

47   to phenotype is challenging. In addition to natural biological variability, these disorders are plagued by

48   variability in penetrance and expressivity[11,12] . Moreover, putatively distinct disorders have amorphous

49   boundaries, overlapping with one another and exhibiting comorbidities[13], as well as sharing genetic

50   origins[14–16] . Collectively, these sources of variation mask the relationships between gene function,

51   circuit organization and neural activity. These same issues make interpretation of studies in animal

52   models similarly challenging.

53   Protocadherin-19 is a member of the δ-protocadherin family of homophilic cell adhesion

54   molecules[17–19] . In humans, mutations in *PCDH19* are linked to schizophrenia and autism[20,21] , and cause

55   a developmental epileptic encephalopathy[22,23]. To investigate how mutations in *pcdh19* or the related

56   *pcdh17* affect neural development, we used visual stimulation and *in vivo* 2-photon calcium imaging in

57   the optic tectum of the larval zebrafish. We show that the neuronal population responses to oriented

58   sinusoidal gratings define neural dynamics that are strongly stereotyped among wild type larvae. In

59   mutants, these dynamics are altered, reflecting stochastic deviations in circuit organization. Our results

60   are consistent with a role for protocadherins in canalization of development, contributing to robustness of

61   circuit assembly. This can provide a conceptual framework for understanding the variability associated

62   with neurodevelopmental disorders.

63

64   ***Results***

65   Moving stimuli, such as moving lines, spots or gratings, elicit robust responses in the optic tectum

66   of zebrafish[24–27]. To record the activity of tectal neurons, we generated a transgenic line that *pan-*

67   neuronally expresses a nuclear localized jGCaMP8s (Histone H2B-GCaMP8s).   These transgenic larvae

68   were mounted in a custom imaging chamber (**Fig. 1a**), and we elicited visual responses by projecting a

69   sequence of drifting sinusoidal gratings (12 directions rotated at 30º intervals) onto an adjacent

70   translucent screen (**Fig. 1b,c**). Two-photon image stacks spanning the optic tectum (7 optical sections at

71   10 µm spacing) were collected at 1 Hz (**Fig. 1d**), allowing us to sample population activity. We used

72   constrained non-negative matrix factorization (CNMF) with CaImAn[28] to automatically segment images

73   and extract fluorescence traces from visually-responsive neurons (**Fig. 1e,f**). For further analysis, the

74   neural responses were averaged across three trials (**Fig. 1g**). Overall, we obtained 2506 visually

75   responsive neurons (n=9).

76   It is now widely understood that sensory processing and motor control are encoded by neuronal

77   population dynamics, rather than the activities of individual neurons[29,30] . These latent dynamics consist

78   of a small number of covariation patterns, or neural modes, which describe a neural manifold within a

79   low-dimensional subspace[31–33] . To explore the structure of tectal population dynamics in response to

80   visual stimulation, we performed linear dimensionality reduction with principal component analysis (PCA)

81   (**Fig. 2a**). For n neurons, PCA reduces the data from an n-dimensional space to a more compact k-

82   dimensional space. We found that the first five neural modes captured 89.9±1.8% (n=9; mean ± sem.) of

83   the variance in our wild type data (**Fig. 2b**), and our subsequent analyses are confined to these five

84   neural modes. Each axis represents a significant pattern of neuronal covariation that is activated to

85   varying extent during the presentation of visual stimuli, and projection of the original neural data onto

86   these axes describes the latent dynamics evoked by visual stimulation (**Fig. 2c**). To determine how

87   consistent the neural responses are in individual larvae, the latent dynamics were obtained for individual

88   trials, and the Pearson's correlation (r) between individual trials was calculated along each dimension

89   (**Fig. 2c,d**). The mean trial-to-trial correlation was greater than 0.9 across all 5 neural modes (**Fig. 2d**).

90   Recent evidence suggests that the similarity of neural architecture among individuals gives rise to similar

91   latent dynamics for a given stimulus or motor task[34] . In mammals, latent dynamics are estimated from a

92   small subsample of neurons, which varies from individual to individual. In such cases, the latent

93   dynamics from different animals need to be aligned using a procedure such as canonical correlation

94   analysis[34,35] . Here, we image a relatively large proportion of visually-responsive neurons and sample

95   among the same neuronal types across different fish, obviating the need for alignment. For each wild

96   type individual, we determined the latent dynamics from trial averaged responses (**Fig. 2e**). To quantify

97   the similarity of the dynamics among the pool of wild types, we generated the averaged response, then

98   calculated Pearson's correlation between this average and the dynamics of each individual (**Fig. 2e,f**).

99   The mean correlation along each neural mode was nearly as high as for trial-to-trial correlations (**Fig.**

100   **2c,d**), indicating that the similarity of dynamics among individuals is comparable to the similarity of

101   successive trials in the same individual. Thus, the latent dynamics elicited by visual stimulation is

102   stereotyped across different zebrafish larvae, facilitating comparisons within and among experimental

103   groups. While the latent dynamics among wild type larvae are strongly correlated, it is possible that the

104   correlation could be improved by further alignment. To test this, we performed Canonical Correlation

105   Analysis (CCA) on our wild type datasets, but found that alignment degraded the correlation of dynamics

106   derived from wild type larvae (*not shown*). When plotted in three dimensions, the latent dynamics from

107   individual larvae describe a rosette shaped trajectory, with each leaf representing the response to a

108   direction of grating drift (**Fig. 2g,h**). The averaged dynamics yielded a smooth trajectory in three

109   dimensions (**Fig. 2i**). Thus, the population response to our simple stimulus presentation, encodes the

110   direction of motion on a neural manifold that is preserved across zebrafish larvae.

111   To investigate the involvement of *pcdh19* in the assembly of visual circuitry we used two, distinct

112   *pcdh19* mutant alleles. We previously introduced an indel lesion near the 5' end of exon1 shortly after

113   the sequence encoding the signal peptide[36,37] , resulting in a complete lack of functional Pcdh19 (*pcdh19*-

114   ^{10bp}). In addition, we have generated a new "promoterless" *pcdh19* allele, which lacks ~4kb of genomic

115   sequence, spanning the basal promoter, 5'UTR and the ATG start codon in exon 1 (*pcdh19$^{\Delta prom}$*)(**Fig.**

116   **S1a,b**). While both alleles completely eliminate the production of Pcdh19 protein (**Fig. S1c**), evidence

117   suggests that indel mutations, like *pcdh19^{-10bp}*, can elicit compensatory mechanisms arising from

118   nonsense-mediated RNA decay[38,39] . Both of these mutant lines were crossed into our *Tg(elav3l:H2B-*

119   *GCaMP8s)* line. As above, we performed calcium imaging on homozygous mutants during visual

120   stimulation, and computed the latent dynamics for each mutant from the trial averages of visually

121   responsive neurons (**Fig. 3a,b**). To determine whether the mutant groups differed from wild type in their

122   visual responses, we correlated the trial-averaged dynamics from each individual mutant with the wild

123   type group average along each neural mode (**Fig. 3c**). Both *pcdh19^{-10bp}* and *pcdh19$^{\Delta prom}$* showed

124   decreased correlation with the group average (**Fig. 3c**), although this varied by neural mode between the

125   two mutants. The *pcdh19^{-10bp}* larvae showed the greatest change along the second neural mode, while

126   *pcdh19$^{\Delta prom}$* mutants exhibited significant differences along neural modes 2-5 (**Fig. 3c**). The response to

127   drifting sinusoidal gratings diverged from wild type for both *pcdh19* mutants, as the trajectories of

128   individual mutant fish were less correlated to the wild type average than were individual wild type fish. To

129   determine whether individual mutants described similar or distinct trajectories, we calculated pairwise

130   correlations between larvae within an experimental group.   If mutants converged on a distinct, but

131   stereotyped, circuit organization, then their intra-group correlation should be similar to the intra-group

132   correlations of the wild type group. Alternatively, if the divergence of the mutants from wild type is due to

133   stochastic variations, then the intra-group correlations should be lower and exhibit an increased variance.

134   Consistent with stochastic variation, the *pcdh19* mutants exhibit lower intra-group correlations than wild

135   type larvae (**Fig. 3d**). When visualized in three dimensions, the trajectories from individual *pcdh19$^{\Delta prom}$*

136   mutants differ dramatically from the stereotyped paths of wild type larvae (**Fig. 2g,h**), and diverge from

137   each other (**Fig. 3e,f**). However, despite the variability of the individual mutants, averaging within a

138   genotype suppresses this variation and gives rise to averaged dynamics that are strongly correlated with

139   wild type (**Fig. 3g**). This suggests that the effect of *pcdh19* loss on visual processing is best understood

140   as stochastic developmental noise, as this noise can be suppressed by averaging (**Fig. 3g**).

141   Pcdh19 is a member of a small family of related δ2-pcdhs. To determine if mutations in other δ2-

142   pcdhs also affect visual responses in the optic tectum, we recorded the response to visual stimulation in

143   mutants lacking *pcdh17* (*pcdh17*$^{-5bp}$)[37] . As above, we used the trial averaged neuronal responses to

144   compute the latent dynamics along the first five neural modes (**Fig. 4a**). Similar to the *pcdh19* mutants,

145   the latent dynamics exhibited by *pcdh17*$^{-5bp}$ mutants was less correlated with the wild type average (**Fig.**

146   **4a**), although the differences were not statistically significant (**Fig. 4b**). To measure the intra-group

147   variation exhibited by the *pcdh17*$^{-5bp}$ mutants, we determined pairwise correlations along each neural

148   mode (**Fig. 4c**). Although there was a uniform decrease in pairwise correlation among the *pcdh17*$^{-5bp}$

149   mutants, this was only significant for neural mode 5 (**Fig. 4c**). This observed intra-group noise was

150   eliminated by averaging, as the *pcdh17*$^{-5bp}$ group average exhibited high correlation with the wild type

151   average (**Fig 4d**). As each mutant genotype showed a reduced intra-group correlation, it is possible that

152   this increased variation is due to unreliable or noisy neuronal responses. To determine whether the

153   tectal responses to visual stimulation are reliable, we determined the between-trial correlations for each

154   neural mode within each experimental group (**Fig. 4e**). We found no significant difference in the

155   between-trial consistency of the population dynamics in the mutant groups, compared to wild type (**Fig.**

156   **4e**). This suggests that each mutant network is responding reliably and reproducibly to repeated

157   presentations of a given stimulus, yet deviates randomly from the wild type. To quantify the within-group

158   variance, we generated histograms of all pairwise correlation coefficients within each experimental group

159   (**Fig. 4f**). While the distribution of correlation coefficients for the wild type group is narrow and

160   concentrated at higher correlations, the mutants all exhibit significantly broader distributions (**Fig. 4f**). To

161   provide a metric for the overall similarity of latent dynamics among different larvae, we calculated the

162   mean r of individual correlations across the five neural modes for each genotype (**Fig. 4g**). If the

163   computed dynamics are empirical estimates of the neural manifold, then this summary r should measure

164   the similarity of an individual manifold to the averaged wild type manifold. In the case of each mutant

165   genotype, the dynamics are significantly different from wild type, although the effect is more robust for

166   the *pcdh19*$^{\Delta prom}$ mutants (**Fig. 4g**). While the variations along individual neural modes are not considered

167   to be statistically significant for the *pcdh17*$^{-5bp}$ mutants, the aggregate impact on the shape of the neural

168   manifold is significant (**Fig. 4g**). Thus, loss of either *pcdh19* or *pcdh17* alters the neural population

169   response to visual stimulation, by introducing stochastic perturbations into circuit assembly. Our data are

170   consistent with the idea that δ2-pcdhs contribute to canalization of the developing optic tectum (**Fig. 4h**).

171   To determine the relationship of the altered latent dynamics in the pcdh mutants to more traditional

172   measures of neuronal responses, we determined the orientation and direction selectivity for neurons in

173   wild type larvae and each of the mutants (**Fig. S2**). For each neuron, we determined an orientation

174   selectivity index (OSI), direction selectivity index (DSI) and preferred direction. The the *pcdh17^{-5bp}*

175   mutants exhibited a dramatic decrease in orientation selectivity (**Fig. S2a**) and direction selectivity (**Fig.**

176   **S2b**), while both *pcdh19^{-10bp}* and *pcdh19$^{\Delta prom}$* showed a shift toward increased orientation selectivity and

177   a modest decrease in direction selectivity in the *pcdh19$^{\Delta prom}$* mutants. The distribution of preferred

178   orientations also exhibited differences among the mutants, as *pcdh17^{-5bp}* mutants exhibited a decreased

179   response to rostral-to-caudal motion (**Fig. S2c,d**), and both *pcdh19^{-10bp}* (**Fig. S2c,e**) and *pcdh19$^{\Delta prom}$*

180   (**Fig. S3c,f**) showed an increase in the proportion of neurons responding to rostral-to-caudal motion.

181   In addition to homozygous mutants, we also analyzed the visual responses of heterozygous

182   mutants (**Fig. S3**). Latent dynamics in the heterozygotes was similar to each of the respective

183   homozygous mutants (**Fig. S3a-c**). Both the correlation of individual neural modes to the wild type

184   average (**Fig. S3d**) and the pairwise, within-group correlations (**Fig. S3e**) were lower than for wild type

185   and the reduction was comparable in magnitude to what we observed in homozygous mutants. When

186   averaged across neural modes, the mean similarity of each δ2-pcdh mutant to the wild type neural

187   response was reduced (**Fig. S3f**), and was characterized by increased within-group variation (**Fig. S3g**).

188   As was observed for homozygous mutants (**Fig. 3,4**), this variability could be averaged away and

189   averages of the heterozygous mutants were highly correlated with the wild type average (**Fig. S3h,i**).

190

191   ***Discussion***

192   The δ2-pcdhs comprise a subfamily of homophilic cell adhesion molecules within the cadherin

193   superfamily, and are associated with neurodevelopmental disorders in humans[40,41]. Among the five δ2-

194   pcdhs in mammals, all are linked to human disorders: *PCDH8* and *PCDH10* are linked to autism[42,43], a

195   genomic deletion encompassing *PCDH18* caused severe intellectual disability[44] , *PCDH17* is implicated

196   in mood disorders[45] , and mutations in *PCDH19* cause a developmental epileptic encephalopathy[22,23] ,

197   and are associated with autism and schizophrenia [20,21] . We previously used large-scale *in vivo* calcium

198   imaging of spontaneous activity and network analysis to show that zebrafish mutants lacking *pcdh19* had

199   defects in network topology[46] . Subsequently, others showed that mutant rodents and zebrafish larvae

200   were hyperexcitable[47,48] , and that mutant rodents showed increased network synchrony[47] . Here, our

201   results show that loss of either *pcdh19* or *pcdh17* impairs visual processing in the optic tectum of the

202   larval zebrafish.

203   Our data show that the response of the larval optic tectum to moving sinusoidal gratings is

204   encoded by low-dimensional dynamics that are confined to a neural manifold. These dynamics are highly

205   stereotyped among wild type individuals. It was recently shown that dynamics are preserved across

206   individuals within a species, but these dynamics need to be aligned using a procedure such as canonical

207   correlation analysis[34], due to the fact that the latent dynamics are estimated from only a small subsample

208   of neurons that vary among animals. Here, we image a substantial proportion of the visually responsive

209   neurons in the optic tectum. Consequently, the dynamics derived from different individuals do not require

210   further alignment. This allows the complex neural responses of hundreds of neurons in different animals

211   to be reduced to a common set of activity patterns that can be quantitatively compared within and

212   between genotypes. The variation among wild type individual larvae is very low, indicating that

213   development within a population gives rise to an ensemble of equivalent networks that differ in the

214   precise number, morphology and connectivity of the constituent neurons, but whose overall functional

215   variation is low.

216   Elimination of either *pcdh19* or *pcdh17* leads to altered latent dynamics. The stereotyped neural

217   response that characterizes the population of wild type larvae is degraded in the mutants, whose

218   dynamics are less well correlated to the averaged wild type response. The latent dynamics among the

219   mutant genotypes varies by individual. As a consequence, within a mutant group, individuals are much

220   less similar to each other than the pool of wild type larvae are to each other. Additionally, this stochastic

221   variability is masked in a group average, as the deviations specific to an individual can be averaged

222   away. This implies that the loss of Pcdh19 or Pcdh17 does not lead to a particular, alternative network

223   structure, but to a stochastic array of alternatives. Thus, the effects of the *pcdh19* and *pcdh17* mutations

224   are best understood as an increase in developmental noise, leading to an increase in phenotypic

225   variability. Our data show that the effects of a well-defined genetic lesion on a simple, highly stereotyped

226   network can be stochastic. While both *pcdh19^{-10bp}* and *pcdh19$^{\Delta prom}$* mutants result in a complete loss of

227   Pcdh19 protein, their effects on the optic tectum are not identical. The phenotype associated with

228   Pcdh19 loss in the *pcdh19$^{\Delta prom}$* line is significantly more severe than in the *pcdh19^{-10bp}* line. Combined

229   with the observation that the magnitude of the impact of indel mutations in *pcdh19^{-10bp}* and *pcdh17^{-5bp}* is

230   similar, this suggests that the difference could be due to the activation of compensatory mechanisms by

231   the indel mutations that are absent in the promoterless allele. This may indicate a further source of

232   variability in understanding neural disorders and in the study of relevant genes in animal models, as even

233   alternative "null" mutations may give rise to distinct phenotypes.

234   In evolution, strong selective pressures prevent the accumulation of mutations that have an

235   adverse impact on phenotypic fitness. Release of a selective pressure can then lead to an increase in

236   allelic and phenotypic diversity within a population. By analogy, our results suggest that Pcdh19 and

237   Pcdh17 suppress variation in the development of tectal circuitry. Loss of either protocadherin releases a

238   constraint on circuit assembly, allowing stochastic variation in circuit organization and function. These

239   results suggest that Pcdh19 and Pcdh17 contribute to developmental robustness by canalizing circuit

240   assembly and limiting developmental variability. While canalization is most commonly discussed in terms

241   of gene regulatory networks buffering against adverse genetic or environmental effects[49,50] , we suggest

242   that the protocadherins may buffer against the formation of inappropriate connections and help guide

243   circuit assembly toward an optimal outcome. These results suggest that while the heterogeneity

244   observed in neurodevelopmental disorders is often attributed to polygenic effects, it could also be due to

245   decanalization of circuit assembly and stochastic degradation of circuit function.

246

247   ***Methods***

248   *Zebrafish maintenance and generation of lines*

249   Adult zebrafish (Danio rerio) were maintained at ~28.5°C and staged according to Westerfield

250   (1995). All animal procedures were performed in accordance with the Ohio State University animal care

251   committee's regulations. We previously generated lines harboring germline mutations of *pcdh19*

252   (*pcdh19os51*)[36] and *pcdh17* (*pcdh17os69*)[37] .

253   The *pcdh19Δprom* mutant line (*pcdh19os77*) was established by co-injecting ribonucleoprotein

254   complexes (Integrated DNA Technologies) consisting of Cas9 protein and gRNAs targeting a site in the

255   5' end of *pcdh19* exon1 (GGGCTCAGATTAACCCATCG) and ~4 kb upstream of the ATG start codon

256   (CTGTTGTGAGCTAGTTACCA), which is predicted to eliminate the promoter region. Founders were

257   identified by PCR and sequenced, confirming the large genomic deletion. Like the *pcdh19-10bp* line,

258   Western blots confirmed that the homozygous *pcdh19Δprom* line produced no Pcdh19 protein.

259   The plasmid *Tol2-elavl3:H2B-GCaMP8s* was assembled using the following plasmids: Tol2-

260   elavl3-GCaMP6s (a gift from Misha Ahrens; Addgene plasmid # 59530 ; http://n2t.net/addgene:59530 ;

261   RRID:Addgene_59530), CMV:Histone H2B-mGL (H2B-mGreenLantern was a gift from Gregory Petsko;

262   Addgene plasmid # 164464 ; http://n2t.net/addgene:164464 ; RRID:Addgene_164464), and

263   CMV:jGCaMP8s (gift from GENIE Project; Addgene plasmid # 162371 ; http://n2t.net/addgene:162371 ;

264   RRID:Addgene_162371). Along with mRNA encoding Tol2 transpose, this plasmid was co-injected into

265   1 cell stage *nacre* embryos in order to establish the transgenic line *Tg(elavl3:H2B-GCaMP)os78*.   This

266   transgenic line was crossed with the *pcdh19-10bp*, *pcdh19Δprom* and *pcdh17-5bp* mutant lines.

267

268   *Calcium imaging*

269   Unanaesthetized 6 days-post-fertilization (dpf) larvae were embedded dorsal side up in 2% low

270   melting point agarose. Imaging was performed on a custom-built resonant-scanning 2-photon

271   microscope. Briefly, 920nm excitation was provided by an Axon920-TPC laser (Coherent, Inc.). We

272   used a Nikon Apochromat 25x/1.1NA water-immersion objective for imaging. The resonant scan-head

273   and controller, 3DMS robotic stage, Hamamatsu GaAsP photomultiplier tubes and power supply were

274   obtained from Sutter Instruments (www.sutter.com). A piezo-electric objective positioner (nPFocus250)

275   was obtained from nPoint (www.npoint.com). The microscope was run with ScanImage 5.2[51] (Vidrio

276   Technologies). All other parts were obtained from Thorlabs (www.thorlabs.com). Image stacks of 7

277   optical sections (512x512), spaced at 10 µm, were collected at 1 s intervals, with a pixel size of 0.65 µm.

278   For each group, we included data from 9-13 larvae, which is in line with the number of fish used in

279   comparable studies[52–54] . These were derived from at least two, separate crosses.

280

281   *Visual stimulation*

282   Visual stimuli were programmed in Python, using PsychoPy3 (https://psychopy.org). Moving sinusoidal

283   gratings were presented for 5 seconds, with 10 seconds of a neutral gray background in between each

284   direction, which were rotated at 30° intervals. The stimulus set was presented three times, with 50

285   seconds in between each presentation. Stimuli were projected onto a translucent screen 2.5 cm from the

286   larvae using a Rif6 cube picoprojector (rif6.com). The stimulus occupied ~104° of the visual field.

287

288   *Data analysis*

289   We used CaImAn-MATLAB for processing of calcium imaging movies[28] , including non-rigid

290   motion correction with NoRMCorre[55] . First, sequences of image stacks (735 stacks of 7 planes) were

291   re-formatted to movies of image planes (7 stacks of 735 timepoints). These were motion corrected and

292   inspected for motion artifacts. Movies that exhibited z-drift or other defects were discarded. Brightness

293   and contrast were adjusted and then images were masked in order to analyze only the left (visually-

294   responsive) hemi-tectum. CaImAn was used to segment movies and extract ΔF/F fluorescence traces.

295   Cells that were responsive to the visual stimuli in each of the three trials were selected for further

296   analysis.

297   Principal Component Analysis was performed on individual datasets. As ~90% of the variance

298   was explained by the top 5 principal components (neural modes), we restricted our analysis to these.

299   We projected the original neural responses onto these new basis vectors. The order of neural modes

300   varied among datasets, as did the sign of the neural mode. We established a standard order and

301   inspected each dataset to ensure a common order and sign for the neural modes. For comparisons of

302 neural modes among datasets, we used Pearson's correlation, r[34,35] . First, we averaged dynamics

303 along each neural mode to generate a wild type average. Correlation of neural modes from individual

304 larvae to the averaged neural modes provided a measure of variation. As an alternative measure of the

305 variation in the datasets, each individual set of neural modes was correlated to all others within a group.

306 This pairwise correlation describes how much latent dynamics varied among individuals within a

307 genotype. To generate a single measure of similarity of latent dynamics between an individual and the

308 wild type average, we averaged the correlation coefficients across the 5 neural modes. For

309 comparisons, statistical significance was determined using Dunnett's test. For the comparison of

310 distributions of r, we used a Dunn's test. To compare circular distributions, we used a MATLAB

311 implementation of Watson's U^2 test (Pierre Mégevand (2025) pierremegevand/watsons_u2

312 https://github.com/pierremegevand/watsons_u2). All other statistical analysis was performed in JMP Pro

313 17.

314

315 *Canonical Correlation Analysis*

316 CCA was implemented in MATLAB and performed as described in Gallego et al. (2018). Briefly, a QR

317 decomposition was performed on each set of dynamics to be aligned ($L_1 = Q_1 R_1$ and $L_2 = Q_2 R_2$), then

318 a singular value decomposition was performed on the inner product of Q_1 and Q_2 ($USV^T = Q_1^T Q_2$). The

319 dynamics were then aligned by $L_2' = L_2 M_2 M_1^{-1}$, where $M_1 = R_1^{-1} U$ and $M_2 = R_2^{-1} V$.
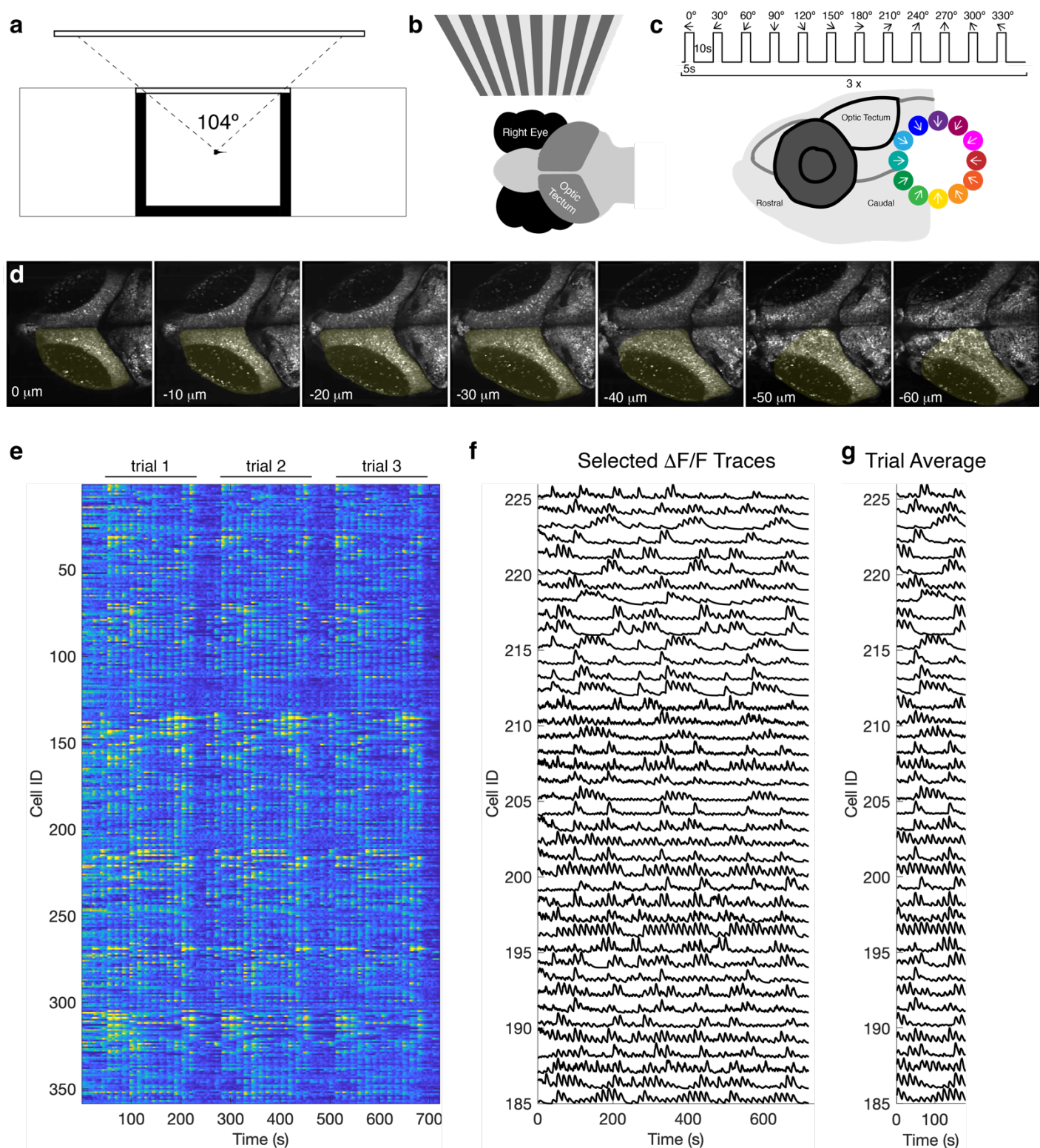
320

321 **Acknowledgements**

328

329

Figure 1. Calcium-imaging of neural responses to oriented sinusoidal gratings.
a. Schematic of the experimental setup. A 6dpf larva is embedded in agarose in an imaging chamber, allowing 104º view of a projection screen.
b. The visual stimuli are presented to the right eye and the neural responses are visualized in the contralateral (left) hemi-tectum.

335   *c. The stimulation protocol is a series of 5s on 10s off of a moving sinusoidal grating, 12 directions spaced at 30º*
336   *intervals to encompass the full 360º. This is repeated three times. Below is a lateral view of the head of a*
337   *zebrafish larva. The inset shows the directions of motion of sinusoidal gratings with reference to the rostro-caudal*
338   *axis of the fish. The direction color-code is used throughout the paper.*
339   *d. Image stacks consisting of 7 optical sections spaced at 10 µm were collected at 1s intervals. Shown are*
340   *average intensity images of individual planes from a timelapse sequence collected in a 6 dpf transgenic larva,*
341   *Tg(elav3l:HistoneH2B-GCaMP8s). The visually-responsive hemi-tectum is outlined in yellow.*
342   *e. Example data showing all the fluorescence traces from visually-responsive neurons collected from one larva.*
343   *f. ΔF/F traces selected from those shown in e.*
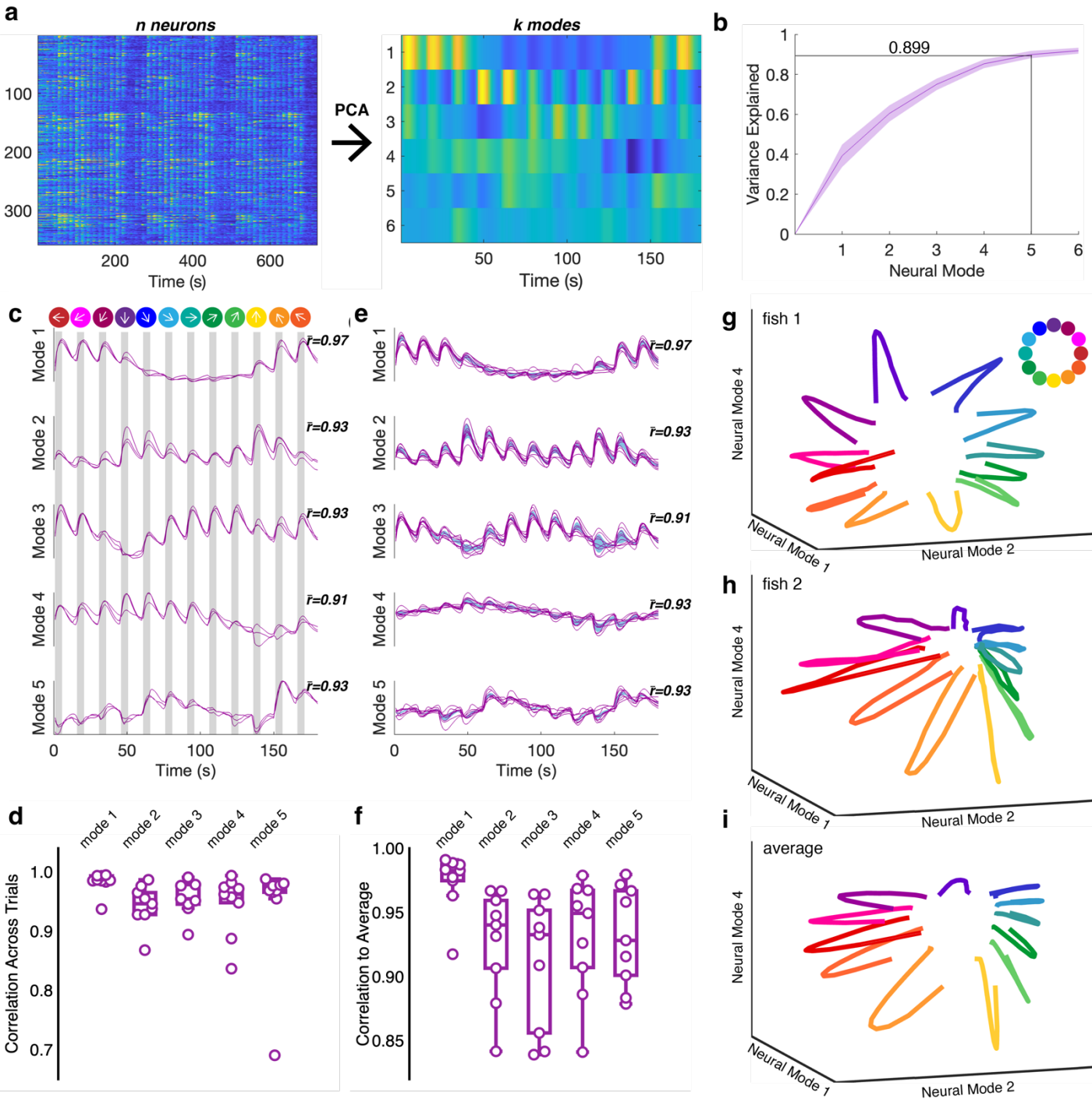344   *g. Responses were averaged across the three trials. Shown are the trial averages from the traces in f.*
345
346
347
348
349
350
351
352
353
354
355
356
357
358
359
360
361
362
363
364
365
366
367
368
369
370
371
372
373
374
375
376
377
378
379
380
381
382

383
384
385
386
387
388
389
390
391
392
393
394

395   ***Figure 2. Latent dynamics in the optic tecta of zebrafish larvae in response to visual stimulation.***

396   ***a.*** *Illustration of our approach to data analysis. Datasets such as the one shown on the left consisted of*
397   *fluorescence traces from n neurons. These were trial averaged and the dimensionality of the trial*
398   *averaged data was reduced using PCA. The new k dimensions are referred to as neural modes.*
399   ***b.*** *The first 5 neural modes explain ~90% of the variance in the data. The shaded area represents the*
400   *standard deviation, n=9).*
401   ***c.*** *Shown are the latent dynamics of an individual wild type larva for the first 5 neural modes. The latent*
402   *dynamics were calculated independently for each of the three trials. The mean correlation of the*
403   *dynamics among the individual trials to the trial average is shown as $\bar{r}$. The presentation of each*
404   *stimulus is shown as a gray bar, and the direction of each stimulus is shown at the top.*
405   ***d.*** *Graph summarizing the mean correlations across trials along each mode for the wild type larvae*
406   *(0.98±0.006, mode 1; 0.94±0.012, mode 2; 0.96±0.01, mode 3; 0.95±0.017, mode 4; 0.94±0.032, mode 5*
407   *;n=9)*
408   ***e.*** *Latent dynamics determined from trial averaged data. Traces (purple) are the dynamics from*
409   *individual larvae and the shaded area (blue) is the variance for the wild type group. The value, $\bar{r}$,*
410   *represents the mean correlation of each individual neural mode to the mean dynamics averaged across*
411   *the group (see **f**).*
412   ***f.*** *Summary of the correlation between individual larvae and the group average along neural modes*
413   *(0.97±0.008, mode 1; 0.93±0.014, mode 2; 0.91±0.017, mode 3; 0.93±0.015, mode 4; 0.93±0.013, mode*
414   *5; n=9).*
415   ***g,h.*** *Three-dimensional representation of latent dynamics for two, individual larvae. Each color*
416   *represents a direction of motion for the visual stimulus. The excursions of neural trajectories during*
417   *stimulus presentation describes a roughly circular neural manifold.*
418   ***i.*** *A three-dimensional representation of latent dynamics averaged across the wild type group (n=9).*
419

420

421

422

423

424

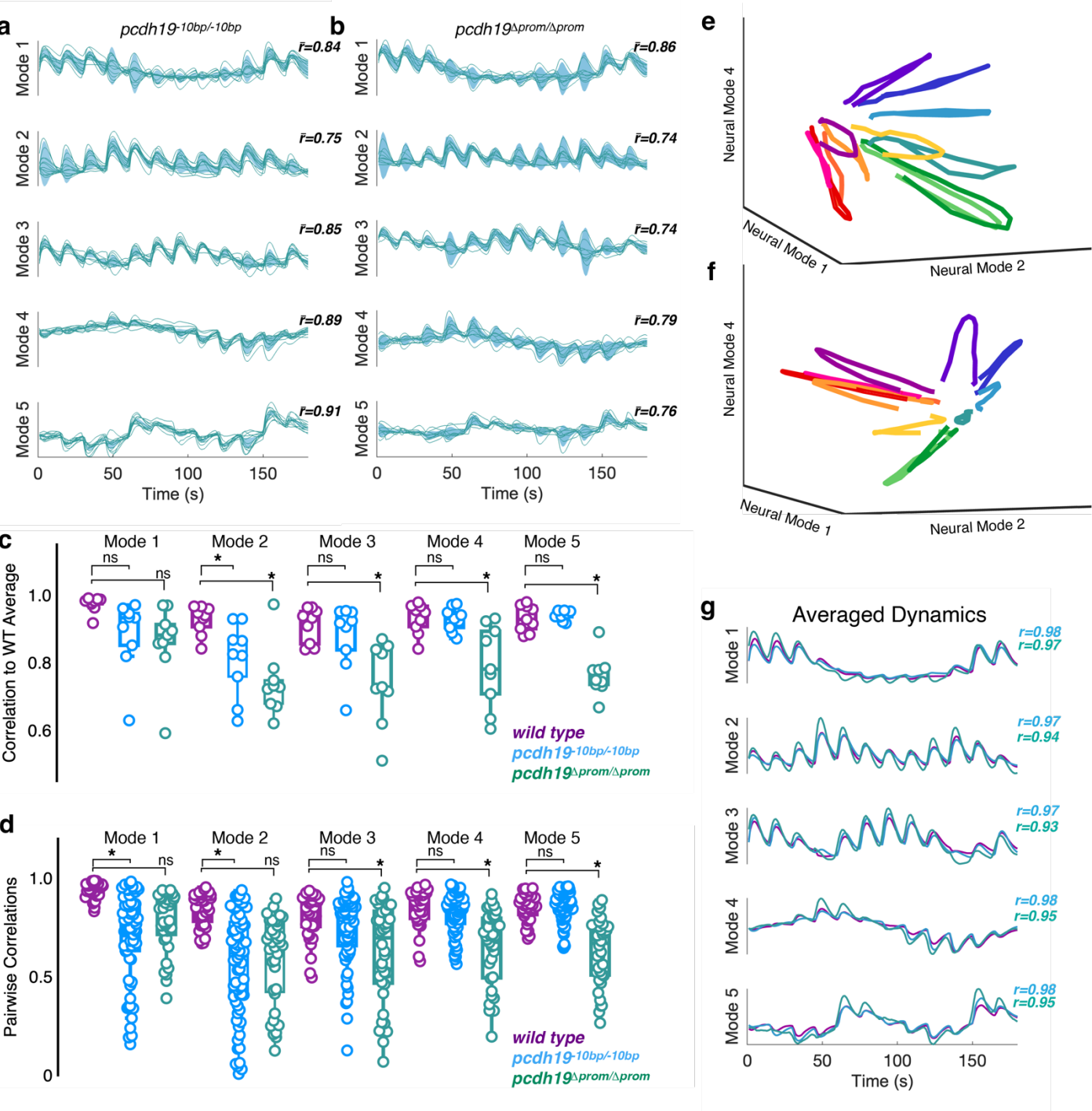**425**

426

427

428

429

430

Figure 3. Mutations in pcdh19 lead to altered neural dynamics.

a,b. Shown are latent dynamics determined from trial averaged neural data collected in homozygous pcdh19^{-10bp} (a) and pcdh19$^{\Delta prom}$ (b) mutant larvae. Individual traces are in teal and the shaded area in blue indicates the group variance. The value, $\bar{r}$, represents the mean correlation of each individual neural mode to the group averaged neural mode. We obtained a total of 3589 visually responsive neurons from pcdh19^{-10bp} larvae, and 2172 neurons from pcdh19$^{\Delta prom}$ larvae.

*c. Boxplot shows the correlation of individual trial-averaged neural modes to the wild type average (wild type, n=9: 0.97±0.008, mode 1; 0.93±0.014, mode 2; 0.91±0.017, mode 3; 0.93±0.015, mode 4; 0.93±0.013, mode 5; pcdh19^{-10bp}, n=12: 0.84±0.035, mode 1; 0.75±0.03, mode 2; 0.85±0.027, mode 3; 0.89±0.014, mode 4; 0.91±0.015, mode 5; pcdh19$^{\Delta prom}$, n=9: 0.88±0.03, mode 1; 0.78±0.04, mode 2; 0.77±0.046, mode 3; 0.80±0.04, mode 4; 0.78±0.022, mode 5; *p<0.05, Dunnett's test).*

*d. Pairwise within-group correlations of neural modes for each genotype (wild type,n=36: 0.94±0.013, mode 1; 0.84±0.028, mode 2; 0.81±0.038, mode 3; 0.85±0.031, mode 4; 0.85±0.023, mode 5; pcdh19^{-10bp}, n=66: 0.71±0.064, mode 1; 0.56±0.076, mode 2; 074±0.051, mode 3; 0.82±0.03, mode 4; 0.86±0.022, mode 5 ; pcdh19$^{\Delta prom}$, n=36: 0.78±0.05, mode 1; 0.59±0.075, mode 2; 0.61±0.095, mode 3; 0.64±0.031, mode 4; 0.63±0.056, mode 5; *p<0.05, Dunnett's test).*

*e,f. Three-dimensional representations of latent dynamics of individual pcdh19$^{\Delta prom}$ mutant larvae. The view is the same as in **Fig. 2g-i**.*

g. Neural modes were averaged within each genotype (wild type/purple, pcdh19^{-10bp}/blue, pcdh19$^{\Delta prom}$/teal. The value, r, represents the correlation of each mutant average with the wild type average (pcdh19^{-10bp}/blue, pcdh19$^{\Delta prom}$/teal).
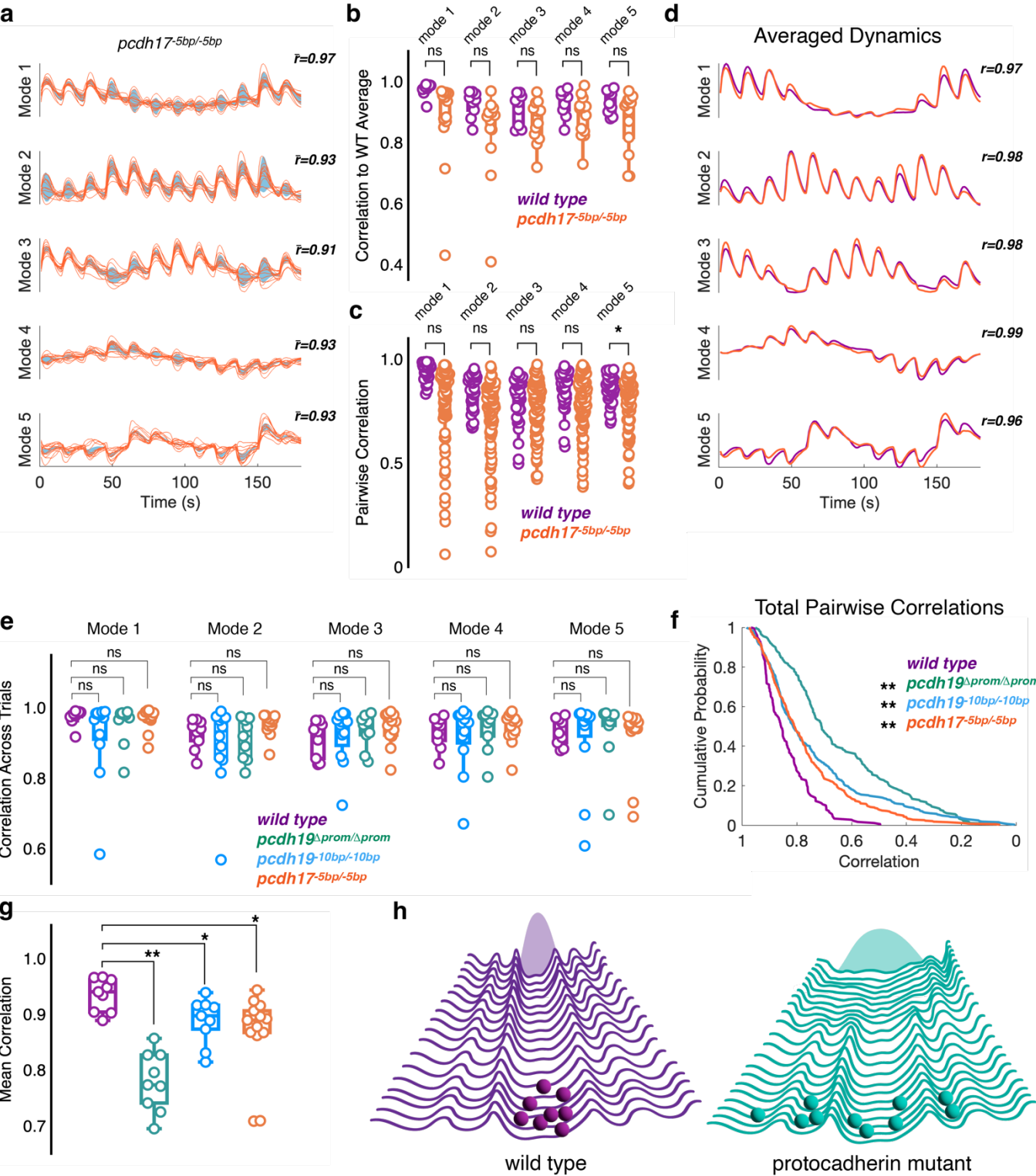
Figure 4. Mutations in pcdh17 lead to altered neural dynamics.

a. *Latent dynamics computed from trial averaged neural data collected in homozygous pcdh17^{-5bp} mutant larvae. Individual traces are in orange and the shaded area in blue indicates the group variance. The value, $\bar{r}$, represents the mean correlation of each individual neural mode to the group average of that neural mode. We obtained a total of 3561 visually-responsive neurons.*

b. *The correlation of individual trial-averaged neural modes to the wild type average (wild type: 0.97±0.008, mode 1; 0.93±0.014, mode 2; 0.91±0.017, mode 3; 0.93±0.015, mode 4; 0.93±0.013, mode 5, n=9; pcdh17^{-5bp}: 0.87±0.042, mode 1; 0.83±0.04, mode 2; 0.87±0.019, mode 3; 0.89±0.027, mode 4; 0.87±0.093, mode 5, n=13).*

c. *Pairwise within-group correlations of neural modes for wild type (purple) and pcdh17 mutants (orange). (wild type, n=36: 0.94±0.013, mode 1; 0.84±0.028, mode 2; 0.81±0.038, mode 3; 0.85±0.031, mode 4; 0.85±0.023, mode 5; pcdh17^{-5bp}, n=78: 0.78±0.055, mode 1; 0.71±0.053, mode 2; 0.77±0.037, mode 3; 0.79±0.039, mode 4; 0.79±0.035, mode 5; *p,0.05, Dunnett's test).*

d. *Neural modes were averaged for pcdh17^{-5bp} mutants (orange) and the average was compared to the wild type average (purple). The value, $\bar{r}$, represents the correlation of each mutant average with the wild type average.*

e. *The mean trial to trial correlations are shown for wild type (purple), pcdh19^{-10bp} (blue) pcdh19$^{\Delta prom}$ (teal), and pcdh17^{-5bp} (orange) mutants. Trial-to-trial variability in the mutants is not statistically different from wild type larvae (wild type, n=9: 0.98±0.006, mode 1; 0.94±0.012, mode 2; 0.96±0.01, mode 3; 0.95±0.017, mode 4; 0.94±0.032, mode 5; pcdh19^{-10bp}: 0.92±0.034, mode 1; 0.89±0.034, mode 2; 0.92±0.022, mode 3; 0.92±0.027, mode 4; 0.91±0.036, mode 5; pcdh19$^{\Delta prom}$: 0.91±0.024, mode 1; 0.90±0.025, mode 2; 0.90±0.025, mode 3; 0.90±0.015, mode 4; 0.85±0.049, mode 5; pcdh17^{-5bp}, n=13: 0.97±0.009, mode 1; 0.95±0.009, mode 2; 0.94±0.013, mode 3; 0.94±0.012, mode 4; 0.92±0.026, mode 5).*

f. *Cumulative probability histogram for the distribution of all pairwise within group r values for wild type (purple), pcdh19^{-10bp} (blue) pcdh19$^{\Delta prom}$ (teal), and pcdh17^{-5bp} (orange) mutants. (**p<0.0001, Dunn's test).*

g. *Mean correlation (r) of individual datasets to the wild type average, averaged across neural modes (wild type, n=9: 0.90±0.018; pcdh19^{-10bp}, n=12: 0.83±0.017; pcdh19$^{\Delta prom}$, n=9: 0.74±0.033; pcdh17^{-5bp}, n=13: 0.82±0.028;*p<0.05, **p<0.0001, Dunnett's test).*

h. *Hypothesized roles of Pcdh19 and Pcdh17 in canalyzing the assembly of visual circuits in the zebrafish optic tectum. In the wild type scenario (left/purple), development is canalized and the outcomes (circuit response to visual stimulation) is restricted, showing a small distribution in outcomes (shaded Gaussian). In the case of protocadherin mutants (right/teal), the developmental landscape is flattened, allowing development to stochastically explore a variety of alternative paths, leading to an increased variation among outcomes (broad shaded distribution).*
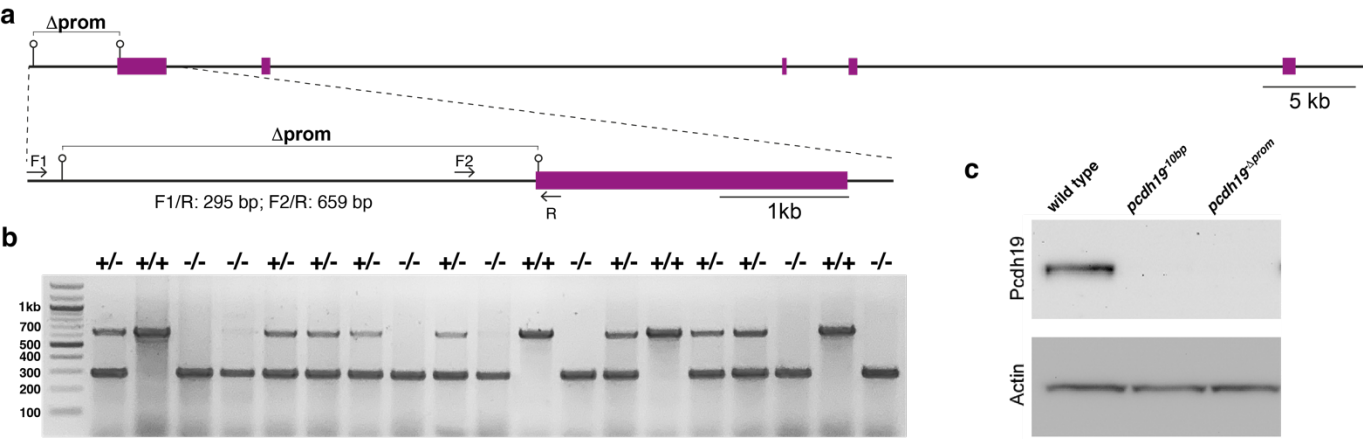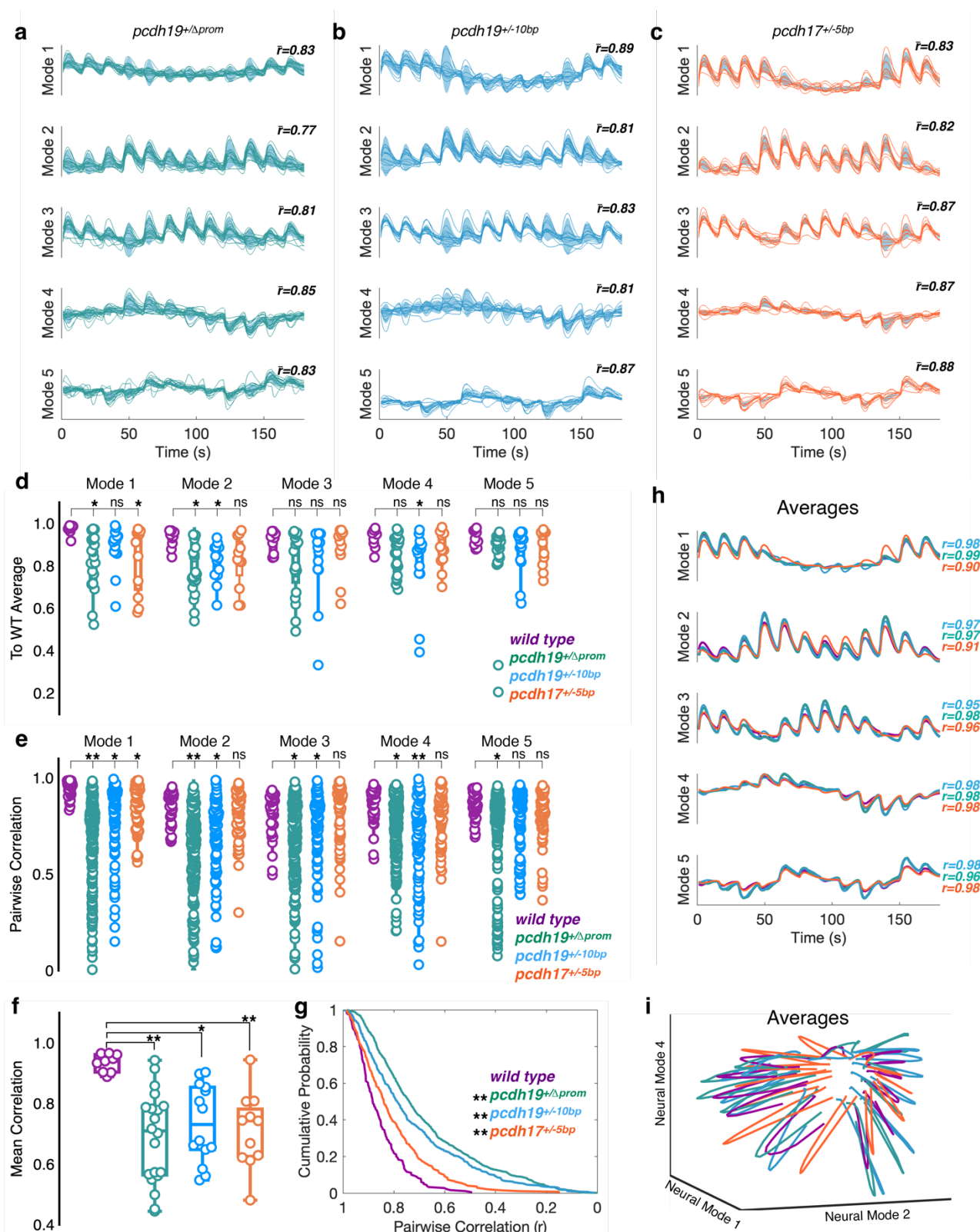
Supplemental Figure 1.
a Schematic of the zebrafish pcdh19 gene, with exons shown in purple. Pins show the sites of CRISPR/Cas9 target sites. Primers used for PCR-based screening are shown, as are the expected sizes of the PCR products.
b Genotyping of mutant in-crosses using F1, F2 and R primers, which distinguish wild type, heterozygous and homozygous mutant larvae.
C Western blot showing the absence of Pcdh19 protein in both our previously published mutant line and in the promoterless line presented here.

Supplemental Figure 2. Heterozygous δ2-pcdh mutants exhibit altered neural dynamics.

a-c. *Latent dynamics computed from trial averaged neural data collected in heterozygous (**a**) pcdh19$^{\Delta prom}$, (**b**) pcdh19^{-10bp} and (**c**) pcdh17^{-5bp} mutant larvae. Individual traces are shown on top of the group variance, shaded in blue. The value, $\bar{r}$, represents the mean correlation of each individual neural mode to the wild type average of that neural mode.*

d. *The correlation of individual trial-averaged neural modes to the wild type average (wild type: 0.97±0.008, mode 1; 0.93±0.014, mode 2; 0.91±0.017, mode 3; 0.93±0.015, mode 4; 0.93±0.013, mode 5, n=9; pcdh19$^{\Delta prom}$: 0.82±0.029, mode 1; 0.77±0.026, mode 2; 0.81±0.033, mode 3; 0.85±0.02, mode 4; 0.83±0.044, mode 5, n=20; pcdh19^{-10bp} : 0.89±0.027, mode 1; 0.81±0.24, mode 2; 0.83±0.047, mode 3; 0.81±0.047, mode 4; 0.87±0.029, mode 5, n=14; pcdh17^{-5bp}: 0.83±0.048, mode 1; 0.82±0.038, mode 2; 0.87±0.036, mode 3; 0.87±0.027, mode 4; 0.88±0.026, mode 5, n=11). (*p<0.05, Dunnett's test).*

e. *Pairwise within-group correlations of neural modes for wild type (purple) and pcdh17 mutants (orange). (wild type, n=36: 0.94±0.007, mode 1; 0.84±0.014, mode 2; 0.81±0.019, mode 3; 0.85±0.016, mode 4; 0.85±0.011, mode 5; pcdh19$^{\Delta prom}$, n=190: 0.66±0.017, mode 1; 0.60±0.016, mode 2; 0.66±0.015, mode 3; 0.74±0.012, mode 4; 0.73±0.016, mode 5 pcdh19^{-10bp} , n=91: 0.8±0.02, mode 1; 0.68±0.022, mode 2; 0.72±0.024, mode 3; 0.65±0.026, mode 4; 0.78±0.017, mode 5; pcdh17^{-5bp}, n=55: 0.84±0.016, mode 1; 080±0.017, mode 2; 0.81±0.0223, mode 3; 0.79±0.022, mode 4; 0.79±0.018, mode 5; **p<0.0001, *p,0.05, Dunnett's test).*

f. *Neural modes were averaged for wild type (purple, 0.9±0.018), pcdh19^{-10bp} (blue, 0.74±0.034), pcdh19$^{\Delta prom}$ (teal, 0.69±0.041) and pcdh17^{-5bp} mutants (orange, 0.71±0.038) and the average was compared to the wild type average (purple). (**p<0.0001, *p<0.05, Dunnett's test).*

g. *Cumulative probability histogram for the distribution of all pairwise within group r values for wild type (purple), pcdh19^{-10bp} (blue) pcdh19$^{\Delta prom}$ (teal), and pcdh17^{-5bp} (orange) mutants. (**p<0.0001, Dunn's test).*

h. *Mean correlation (r) of individual datasets to the wild type average, averaged across neural modes (wild type, n=9: 0.90±0.018; pcdh19^{-10bp}, n=12: 0.83±0.017; pcdh19$^{\Delta prom}$, n=9: 0.74±0.033; pcdh17^{-5bp}, n=13: 0.82±0.028;*p<0.05, **p<0.0001, Dunnett's test).*

i. *Plotting of averaged dynamics along neural modes 1, 2 and 4 for wild type (purple), pcdh19^{-10bp} (blue) pcdh19$^{\Delta prom}$ (teal), and pcdh17^{-5bp} (orange) heterozygous mutants.*

644
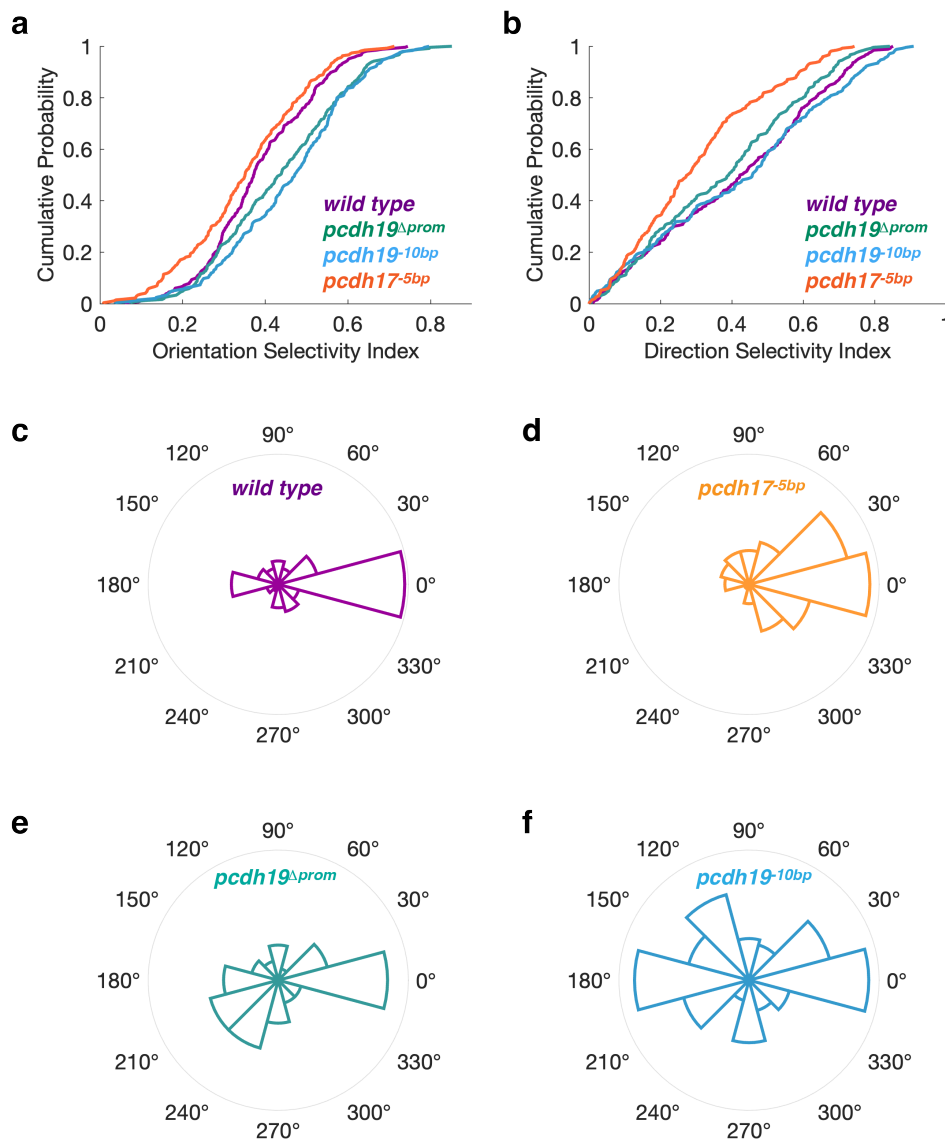
645
646
647
648 **Supplemental Figure 3. Altered orientation selectivity and direction selectivity in δ2-pcdh**
649 **mutants.**
650 *a. Cumulative probability distributions of orientation selectivity for all neurons in wild type (purple),*
651 *pcdh19^{-10bp} (blue) pcdh19$^{\Delta prom}$ (teal), and pcdh17^{-5bp} (orange) mutants. Pcdh17 and Pcdh19 mutants*
652 *exhibit distinct effects on orientation selectivity, with pcdh17^{-5bp} mutants exhibiting an overall shift toward*
653 *reduced orientation selectivity, and both pcdh19^{-10bp} and pcdh19$^{\Delta prom}$ showing a shift toward increased*
654 *direction selectivity.(**p<0.0001; Dunn's test). b. Cumulative probability distributions of direction*
655 *selectivity for all neurons in wild type (purple), pcdh19^{-10bp} (blue) pcdh19$^{\Delta prom}$ (teal), and pcdh17^{-5bp}*
656 *(orange) mutants. The pcdh17^{-5bp} mutants exhibit a dramatic shift toward reduced direction selectivity.*
657 *In contrastboth pcdh19^{-10bp} and pcdh19$^{\Delta prom}$ showing a shift toward increased direction*
658 *selectivity.(*p<0.05, **p<0.0001; Dunn's test).*
659 *c. A polar histogram showing the preferred directions of direction selective neurons (DSI>0.33) in wild*
660 *type larvae. The preferred direction as obtained as the vector average of the responses across all*
661 *stimuli.*

d. A polar histogram showing the preferred direction of direction selective neurons in pcdh17^{-5bp} mutants. There is an increase in the number of cells that prefer caudal-to-rostral motion (p<0.0001; Watson's U2 test).

e. A polar histogram showing the preferred direction of direction selective neurons in pcdh19$^{\Delta prom}$ mutants. There is a slight decrease in cells responsive to caudal-to-rostral motion and an increase in the number of cells that prefer motion between 195º-240º (p<0.0001; Watson's U2 test).

f. A polar histogram showing the preferred direction of direction selective neurons in pcdh19^{-10bp} mutants. There is a large increase in the proportion of cells responsive to directions other than caudal-to-rostral motion, particularly directions centered around 120º and 180º (p<0.0001; Watson's U2 test).

REFERENCES

1. Waddington, C. (1942). Canalization of development and the inheritance of acquired characters. Nature *150*, 563–565. https://doi.org/10.1007/s00128-015-1540-6.

2. Xu, T., Nenning, K.-H., Schwartz, E., Hong, S.-J., Vogelstein, J.T., Goulas, A., Fair, D.A., Schroeder, C.E., Margulies, D.S., Smallwood, J., et al. (2020). Cross-species functional alignment reveals evolutionary hierarchy within the connectome. NeuroImage *223*, 117346. https://doi.org/10.1016/j.neuroimage.2020.117346.

3. Mars, R.B., Sotiropoulos, S.N., Passingham, R.E., Sallet, J., Verhagen, L., Khrapitchev, A.A., Sibson, N., and Jbabdi, S. (2018). Whole brain comparative anatomy using connectivity blueprints. eLife *7*, e35237. https://doi.org/10.7554/elife.35237.

4. Kitano, H. (2004). Biological robustness. Nature reviews Genetics *5*, 826–837. https://doi.org/10.1038/nrg1471.

5. Masel, J., and Siegal, M.L. (2009). Robustness: mechanisms and consequences. Trends Genet. *25*, 395–403. https://doi.org/10.1016/j.tig.2009.07.005.

6. Geschwind, D.H., and Levitt, P. (2007). Autism spectrum disorders: developmental disconnection syndromes. Current opinion in neurobiology *17*, 103–111. https://doi.org/10.1016/j.conb.2007.01.009.

7. Yamasaki, T., Maekawa, T., Fujita, T., and Tobimatsu, S. (2017). Connectopathy in Autism Spectrum Disorders: A Review of Evidence from Visual Evoked Potentials and Diffusion Magnetic Resonance Imaging. Frontiers in neuroscience *11*, 158–14. https://doi.org/10.3389/fnins.2017.00627.

8. Lynall, M.-E., Bassett, D.S., Kerwin, R., McKenna, P.J., Kitzbichler, M., Müller, U., and Bullmore, E. (2010). Functional connectivity and brain networks in schizophrenia. Journal of Neuroscience *30*, 9477–9487. https://doi.org/10.1523/jneurosci.0333-10.2010.

9. Friston, K., Brown, H.R., Siemerkus, J., and Stephan, K.E. (2016). The dysconnection hypothesis (2016). Schizophrenia Research *176*, 83–94. https://doi.org/10.1016/j.schres.2016.07.014.

10. Belmonte, M.K., Allen, G., Beckel-Mitchener, A., Boulanger, L.M., Carper, R.A., and Webb, S.J. (2004). Autism and abnormal development of brain connectivity. Journal of Neuroscience *24*, 9228–9231. https://doi.org/10.1523/jneurosci.3340-04.2004.

11. Woodbury-Smith, M., Nicolson, R., Zarrei, M., Yuen, R.K.C., Walker, S., Howe, J., Uddin, M., Hoang, N., Buchanan, J.A., Chrysler, C., et al. (2017). Variable phenotype expression in a family segregating microdeletions of the NRXN1 and MBD5 autism spectrum disorder susceptibility genes. npj Genom. Med. *2*, 17. https://doi.org/10.1038/s41525-017-0020-9.

12. Masfrand, S. de, Cogné, B., Nizon, M., Deb, W., Goldenberg, A., Lecoquierre, F., Nicolas, G., Bournez, M., Vitobello, A., Mau-Them, F.T., et al. (2024). Penetrance, variable expressivity and monogenic neurodevelopmental disorders. Eur. J. Méd. Genet. *69*, 104932. https://doi.org/10.1016/j.ejmg.2024.104932.

13. Chien, Y., Wu, C., and Tsai, H. (2021). The Comorbidity of Schizophrenia Spectrum and Mood Disorders in Autism Spectrum Disorder. Autism Res. *14*, 571–581. https://doi.org/10.1002/aur.2451.

14. Cristino, A.S., Williams, S.M., Hawi, Z., An, J.-Y., Bellgrove, M.A., Schwartz, C.E., Costa, L. da F., and Claudianos, C. (2013). Neurodevelopmental and neuropsychiatric disorders represent an interconnected molecular system. Molecular psychiatry *19*, 294–301. https://doi.org/10.1038/mp.2013.16.

15. Hamlyn, J., Duhig, M., McGrath, J., and Scott, J. (2013). Modifiable risk factors for schizophrenia and autism - Shared risk factors impacting on brain development. Neurobiology of disease *53*, 3–9. https://doi.org/10.1016/j.nbd.2012.10.023.

16. Zhu, X., Need, A.C., Petrovski, S., and Goldstein, D.B. (2014). One gene, many neuropsychiatric disorders: lessons from Mendelian diseases. Nature Publishing Group *17*, 773–781. https://doi.org/10.1038/nn.3713.

17. Hulpiau, P., and Roy, F.V. (2009). Molecular evolution of the cadherin superfamily. The international journal of biochemistry & cell biology *41*, 349–369. https://doi.org/10.1016/j.biocel.2008.09.027.

18. Nollet, F., Kools, P., and Roy, F. van (2000). Phylogenetic analysis of the cadherin superfamily allows identification of six major subfamilies besides several solitary members. Journal of Molecular Biology *299*, 551–572. https://doi.org/10.1006/jmbi.2000.3777.

741 19. Jontes, J.D. (2017). The Cadherin Superfamily in Neural Circuit Assembly. Cold Spring Harbor
742 perspectives in biology *10*, a029306. https://doi.org/10.1101/cshperspect.a029306.

743 20. Piton, A., Gauthier, J., Hamdan, F.F., Lafrenière, R.G., Yang, Y., Henrion, E., Laurent, S., Noreau,
744 A., Thibodeau, P., Karemera, L., et al. (2011). Systematic resequencing of X-chromosome synaptic genes
745 in autism spectrum disorder and schizophrenia. Molecular psychiatry *16*, 867–880.
746 https://doi.org/10.1038/mp.2010.54.

747 21. Vlaskamp, D.R.M., Bassett, A.S., Sullivan, J.E., Robblee, J., Sadleir, L.G., Scheffer, I.E., and
748 Andrade, D.M. (2019). Schizophrenia is a later-onset feature of PCDH19Girls Clustering Epilepsy.
749 Epilepsia *60*, 429–440. https://doi.org/10.1111/epi.14678.

750 22. Dibbens, L.M., Tarpey, P.S., Hynes, K., Bayly, M.A., Scheffer, I.E., Smith, R., Bomar, J., Sutton, E.,
751 Vandeleur, L., Shoubridge, C., et al. (2008). X-linked protocadherin 19 mutations cause female-limited
752 epilepsy and cognitive impairment. Nature Genetics *40*, 776–781. https://doi.org/10.1038/ng.149.

753 23. Depienne, C., Depienne, C., Bouteiller, D., Bouteiller, D., Keren, B., Keren, B., Cheuret, E., Cheuret,
754 E., Poirier, K., Poirier, K., et al. (2009). Sporadic Infantile Epileptic Encephalopathy Caused by
755 Mutations in PCDH19 Resembles Dravet Syndrome but Mainly Affects Females. PLoS Genetics *5*,
756 e1000381. https://doi.org/10.1371/journal.pgen.1000381.t001.

757 24. Bollmann, J.H., and Engert, F. (2009). Subcellular Topography of Visually Driven Dendritic Activity
758 in the Vertebrate Visual System. Neuron *61*, 895–905. https://doi.org/10.1016/j.neuron.2009.01.018.

759 25. Niell, C.M., and Smith, S.J. (2005). Functional imaging reveals rapid development of visual response
760 properties in the zebrafish tectum. Neuron *45*, 941–951. https://doi.org/10.1016/j.neuron.2005.01.047.

761 26. Baier, H., and Scott, E.K. (2024). The Visual Systems of Zebrafish. Annu. Rev. Neurosci. *47*, 255–
762 276. https://doi.org/10.1146/annurev-neuro-111020-104854.

763 27. Förster, D., Helmbrecht, T.O., Mearns, D.S., Jordan, L., Mokayes, N., and Baier, H. (2020).
764 Retinotectal circuitry of larval zebrafish is adapted to detection and pursuit of prey. Elife *9*, e58596.
765 https://doi.org/10.7554/elife.58596.

766 28. Giovannucci, A., Friedrich, J., Gunn, P., Kalfon, J., Brown, B.L., Koay, S.A., Taxidis, J., Najafi, F.,
767 Gauthier, J.L., Zhou, P., et al. (2019). CaImAn an open source tool for scalable calcium imaging data
768 analysis. eLife *8*, e38173. https://doi.org/10.7554/elife.38173.

769 29. Vyas, S., Golub, M.D., Sussillo, D., and Shenoy, K.V. (2020). Computation Through Neural
770 Population Dynamics. Annu Rev Neurosci *43*, 249–275. https://doi.org/10.1146/annurev-neuro-092619-
771 094115.

772 30. Saxena, S., and Cunningham, J.P. (2019). Towards the neural population doctrine. Curr. Opin.
773 Neurobiol. *55*, 103–111. https://doi.org/10.1016/j.conb.2019.02.002.

774 31. Langdon, C., Genkin, M., and Engel, T.A. (2023). A unifying perspective on neural manifolds and
775 circuits for cognition. Nat. Rev. Neurosci. *24*, 363–377. https://doi.org/10.1038/s41583-023-00693-x.

32. Sadtler, P.T., Quick, K.M., Golub, M.D., Chase, S.M., Ryu, S.I., Tyler-Kabara, E.C., Yu, B.M., and Batista, A.P. (2014). Neural constraints on learning. Nature *512*, 423–426. https://doi.org/10.1038/nature13665.

33. Gallego, J.A., Perich, M.G., Miller, L.E., and Solla, S.A. (2017). Neural Manifolds for the Control of Movement. Neuron *94*, 978–984. https://doi.org/10.1016/j.neuron.2017.05.025.

34. Safaie, M., Chang, J.C., Park, J., Miller, L.E., Dudman, J.T., Perich, M.G., and Gallego, J.A. (2023). Preserved neural dynamics across animals performing similar behaviour. Nature *623*, 765–771. https://doi.org/10.1038/s41586-023-06714-0.

35. Gallego, J.A., Perich, M.G., Chowdhury, R.H., Solla, S.A., and Miller, L.E. (2020). Long-term stability of cortical population dynamics underlying consistent behavior. Nat. Neurosci. *23*, 260–270. https://doi.org/10.1038/s41593-019-0555-4.

36. Cooper, S.R., Emond, M.R., Duy, P.Q., Liebau, B.G., Wolman, M.A., and Jontes, J.D. (2015). Protocadherins control the modular assembly of neuronal columns in the zebrafish optic tectum. J Cell Biol *211*, 807–814. https://doi.org/10.1083/jcb.201507108.

37. Biswas, S., Emond, M.R., Chenoweth, K.P., and Jontes, J.D. (2021). δ-Protocadherins regulate neural progenitor cell division by antagonizing Ryk and Wnt/β-catenin signaling. Iscience *24*, 102932. https://doi.org/10.1016/j.isci.2021.102932.

38. El-Brolosy, M.A., Kontarakis, Z., Rossi, A., Kuenne, C., Günther, S., Fukuda, N., Kikhi, K., Boezio, G.L.M., Takacs, C.M., Lai, S.-L., et al. (2019). Genetic compensation triggered by mutant mRNA degradation. Nature *568*, 193–197. https://doi.org/10.1038/s41586-019-1064-z.

39. Rossi, A., Kontarakis, Z., Gerri, C., Nolte, H., Hölper, S., Krüger, M., and Stainier, D.Y.R. (2015). Genetic compensation induced by deleterious mutations but not gene knockdowns. Nature *524*, 230–233. https://doi.org/10.1038/nature14580.

40. Redies, C., Hertel, N., and Hübner, C.A. (2012). Cadherins and neuropsychiatric disorders. Brain research *1470*, 130–144. https://doi.org/10.1016/j.brainres.2012.06.020.

41. Hirano, S., and Takeichi, M. (2012). Cadherins in Brain Morphogenesis and Wiring. Physiological reviews *92*, 597–634. https://doi.org/10.1152/physrev.00014.2011.

42. Tsai, N.-P., Wilkerson, J.R., Guo, W., Maksimova, M.A., Demartino, G.N., Cowan, C.W., and Huber, K.M. (2012). Multiple Autism-Linked Genes Mediate Synapse Elimination via Proteasomal Degradation of a Synaptic Scaffold PSD-95. Cell *151*, 1581–1594. https://doi.org/10.1016/j.cell.2012.11.040.

43. Morrow, E.M., Morrow, E.M., Yoo, S.-Y., Yoo, S.-Y., Flavell, S.W., Flavell, S.W., Kim, T.-K., Kim, T.-K., Lin, Y., Lin, Y., et al. (2008). Identifying autism loci and genes by tracing recent shared ancestry. Science (New York, NY) *321*, 218–223. https://doi.org/10.1126/science.1157657.

44. Kasnauskiene, J., Kasnauskiene, J., Ciuladaite, Z., Ciuladaite, Z., Preiksaitiene, E., Preiksaitiene, E., Matulevičienė, A., Matulevičienė, A., Alexandrou, A., Alexandrou, A., et al. (2012). A single gene

811 deletion on 4q28.3: PCDH18 - A new candidate gene for intellectual disability? European Journal of
812 Medical Genetics *55*, 1–4. https://doi.org/10.1016/j.ejmg.2012.02.010.

813 45. Chang, H., Hoshina, N., Zhang, C., Ma, Y., Cao, H., Wang, Y., Wu, D., Bergen, S.E., n, M.L. eacute,
814 Hultman, C.M., et al. (2017). The protocadherin 17 gene affects cognition, personality, amygdala
815 structure and function, synapse development and risk of major mood disorders. Molecular psychiatry *23*,
816 1–13. https://doi.org/10.1038/mp.2016.231.

817 46. Light, S.E.W., and Jontes, J.D. (2019). Multiplane calcium imaging reveals disrupted development of
818 network topology in zebrafish pcdh19 mutants. Eneuro *6*, ENEURO.0420-18.2019.
819 https://doi.org/10.1523/eneuro.0420-18.2019.

820 47. Giansante, G., Mazzoleni, S., Zippo, A.G., Ponzoni, L., Ghilardi, A., Maiellano, G., Lewerissa, E.,
821 Hugte, E. van, Kasri, N.N., Francolini, M., et al. (2023). Neuronal network activity and connectivity are
822 impaired in a conditional knockout mouse model with PCDH19 mosaic expression. Mol Psychiatr, 1–16.
823 https://doi.org/10.1038/s41380-023-02022-1.

824 48. Robens, B.K., Yang, X., McGraw, C.M., Turner, L.H., Robens, C., Thyme, S., Rotenberg, A., and
825 Poduri, A. (2022). Mosaic and non-mosaic protocadherin 19 mutation leads to neuronal hyperexcitability
826 in zebrafish. Neurobiol Dis *169*, 105738–105738. https://doi.org/10.1016/j.nbd.2022.105738.

827 49. Hallgrimsson, B., Green, R.M., Katz, D.C., Fish, J.L., Bernier, F.P., Roseman, C.C., Young, N.M.,
828 Cheverud, J.M., and Marcucio, R.S. (2019). The developmental-genetics of canalization. Semin. Cell
829 Dev. Biol. *88*, 67–79. https://doi.org/10.1016/j.semcdb.2018.05.019.

830 50. Siegal, M.L., and Bergman, A. (2002). Waddington's canalization revisited: developmental stability
831 and evolution. Proceedings of the National Academy of Sciences of the United States of America *99*,
832 10528–10532. https://doi.org/10.1073/pnas.102303999.

833 51. Pologruto, T.A., Sabatini, B.L., and Svoboda, K. (2003). ScanImage: flexible software for operating
834 laser scanning microscopes. Biomedical engineering online *2*, 13. https://doi.org/10.1186/1475-925x-2-
835 13.

836 52. Romano, S.A., Pietri, T., Pérez-Schuster, V., Jouary, A., Haudrechy, M., and Sumbre, G. (2015).
837 Spontaneous Neuronal Network Dynamics Reveal Circuit's Functional Adaptations for Behavior. Neuron
838 *85*, 1070–1085. https://doi.org/10.1016/j.neuron.2015.01.027.

839 53. Avitan, L., Pujic, Z., Mölter, J., Poll, M.V.D., Sun, B., Teng, H., Amor, R., Scott, E.K., and Goodhill,
840 G.J. (2017). Spontaneous Activity in the Zebrafish Tectum Reorganizes over Development and Is
841 Influenced by Visual Experience. Current Biology *27*, 2407-2419.e4.
842 https://doi.org/10.1016/j.cub.2017.06.056.

843 54. Gabriel, J.P., Trivedi, C.A., Maurer, C.M., Ryu, S., and Bollmann, J.H. (2012). Layer-specific
844 targeting of direction-selective neurons in the zebrafish optic tectum. Neuron *76*, 1147–1160.
845 https://doi.org/10.1016/j.neuron.2012.12.003.

846   55. Pnevmatikakis, E.A., and Giovannucci, A. (2017). NoRMCorre: An online algorithm for piecewise
847   rigid motion correction of calcium imaging data. Journal of neuroscience methods *291*, 83–94.
848   https://doi.org/10.1016/j.jneumeth.2017.07.031.

849